Acta Oceanol. Sin., 2022, Vol. 41, No. 10, P. 32–40
https://doi.org/10.1007/s13131-022-2007-3
http://www.aosocean.com
E-mail: ocean2@hyxb.org.cn

Tide-induced Lagrangian residual velocity and dynamic analysis based on field observations in the inner Xiangshan Bay, China

Xiaoxuan Sheng[1, 2], Qi Quan[3], Jinzhen Yu[4], Xinyan Mao[1, 2*], Wensheng Jiang[1, 4]

[1] Key Laboratory of Physical Oceanography, Ministry of Education, Qingdao 266100, China

[2] College of Oceanic and Atmospheric Sciences, Ocean University of China, Qingdao 266100, China

[3] State Key Laboratory of Estuarine and Coastal Research, East China Normal University, Shanghai 200241, China

[4] Key Laboratory of Marine Environment and Ecology, Ocean University of China, Qingdao 266100, China

Received 8 October 2021; accepted 20 December 2021

Abstract

In the Xiangshan Bay at the east coast of China, coastal marine pollution is conspicuous and severe in recent years. As transport of the pollutants is closely related to the coastal circulation, there is a great practical significance to investigate the circulation in this area. In this work, the surface pattern and vertical profiles of Lagrangian residual velocity (LRV) were studied based on field observation data from the inner Xiangshan Bay. By tracking GPS-GPRS drifters' trajectories, the surface LRV pattern is going out in the central deep trough and flowing inwards near the shoreside. Combined with data from two mooring stations, vertical profiles of LRV is flowing out at surface and flowing in at the bottom, consistent with the gravitational circulation induced by baroclinic effects at the estuary. However, according to the diagnostic analysis, the main mechanism driving the residual current is barotropic rather than baroclinic. The LRV equation is controlled by the tidally-averaged barotropic pressure gradient force, tidal body force and tidally-averaged turbulent stress, while the tidally-averaged baroclinic pressure gradient force is one order of magnitude less than other forces. Additionally, the tidally mean eddy viscosity coefficient which is used in the expression of tidally-averaged turbulent stress might be not adequate and requires further studies.

Key words: Lagrangian residual velocity, GPS-GPRS drifters, mooring observation, Xiangshan Bay

Citation: Sheng Xiaoxuan, Quan Qi, Yu Jinzhen, Mao Xinyan, Jiang Wensheng. 2022. Tide-induced Lagrangian residual velocity and dynamic analysis based on field observations in the inner Xiangshan Bay, China. Acta Oceanologica Sinica, 41(10): 32–40, doi: 10.1007/s13131-022-2007-3

1 Introduction

The coastal circulation is important to the marine environment in shallow seas, bays and tidal estuaries (Hill et al., 2008; Schulz and Umlauf, 2016; Grifoll et al., 2020; Haid et al., 2020). The Xiangshan Bay is an important aquaculture base and port on the east coast of China (Fig. 1a), where eutrophication and heavy metal pollution have increased seriously in recent years (Sun et al., 2014; Chen et al., 2018; Zhao et al., 2018; Liu et al., 2019). The Xiangshan Bay displays a strong tide, calm wind and a significant tide-induced residual current. Therefore, it is important to study the tidally residual current in the Xiangshan Bay, as it is critical for reducing eutrophication and improving the marine environment.

Two tidally averaged methods can be used to get the tide-induced residual current. The first one is by averaging the tidal current at a fixed spatial point in a tidal cycle, and thus the Eulerian residual velocity (ERV) is obtained (Abbott, 1960; Lavelle et al., 1991; Huijts et al., 2009; Stashchuk et al., 2017). The second one is by averaging the tidal current of a fixed water parcel in a tidal cycle (Zimmerman, 1979; Delhez, 1996; Feng et al., 2008; Cheng, 2020), so the residual current is called the Lagrangian residual velocity (LRV). Most of previous studies on the residual current in the Xiangshan Bay are based on the concept of ERV derived from either *in-situ* observations (Dong and Su, 2000) or numerical simulation (Zhu, 2009; Wan et al., 2015). Results have shown that the ERV pattern is gravitational circulation in the inner bay (west of the Xihu Bay, Fig. 1b), horizontal circulation outside of the bay (the Fodu Channel and Niubi Channel in Fig. 1b), and a mix of the two in the transition area (between the Xihu Bay and the bay mouth). Additionally, several numerical studies on LRV in the Xiangshan Bay have been conducted. Liang et al. (2014) presented the simulated LRV pattern of outflow at the surface and inflow at bottom in the inner Xiangshan Bay. It is similar to the gravitational circulation in the estuary, but the driving forces were not mentioned in that study. In another numerical study of Xu et al. (2016), the LRV in the outer Xiangshan Bay (from 121.8°E to the channels) was shown to be distributed into two branches (Fig. 1b) that may connect the Fodu Channel and Niubi Channel and thus facilitate water exchange. Han et al. (2014) used both ERV and LRV to describe circulation and mass transport. Nevertheless, the circulation and mass transport should be unified rather than split when describing long-term transport in the coastal ocean. In this respect, LRV is more appropriate because it has been proved to satisfy the conservation law of material sur-

Foundation item: The National Natural Science Foundation of China under contract No. 41630966; the Youth Talent Support Program of the Laboratory for Marine Ecology and Environmental Science, Pilot National Laboratory for Marine Science and Technology (Qingdao) under contract No. LMEES-YTSP-2018-02-03.

*Corresponding author, E-mail: maoxinyan@ouc.edu.cn

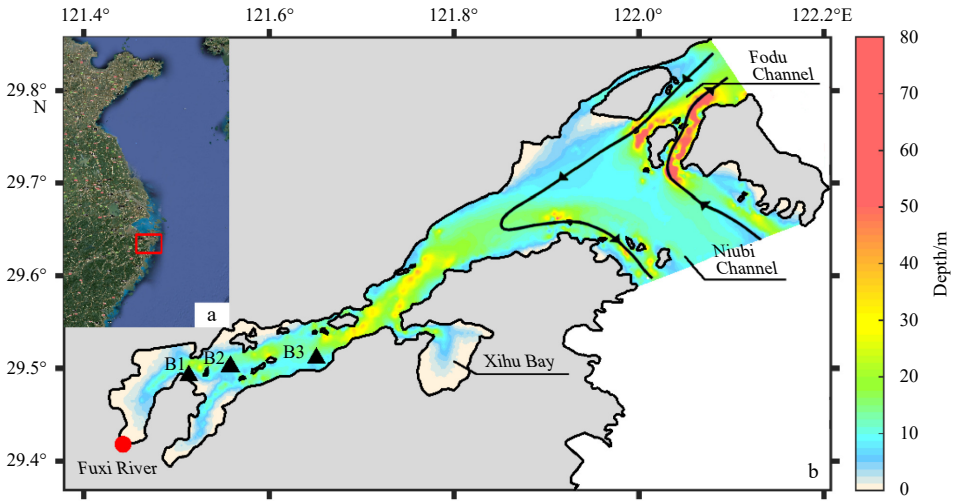

Fig. 1. Satellite image of the East China Sea (a) and bathymetry of the Xiangshan Bay and mooring stations (b). In a, the red box shows the port of the Xiangshan Bay in b; in b, red circle shows the Fuxi River mouth, black triangles represent the mooring stations, and two lines in the Fodu Channel and Niubi Channel represent the result of Lagrangian residual velocity streamlines in Xu et al. (2016).

face (Feng, 1987).

With the development of instruments and technologies, it has been realizable to track drifting buoys for several days and even months and therefore the circulation (e.g., tide-induced LRV) and long-term mass transport can be obtained more directly (Jiang and Sun, 2002; Charria et al., 2013; Callies et al., 2017; Tamtare et al., 2021). In the Xiangshan Bay, a coastal acoustic tomography system was once applied to map the distribution of M_2 and M_4 tidal currents (Chen et al., 2021), which provides us a new idea and dataset to acquire the tide-induced residual current. Besides, more and more studies tend to combine the tracking observations with conventional station observation, in order to fully and conveniently analyze coastal hydrodynamics (Röhrs et al., 2012; Clarke and Van Gorder, 2018).

It should be noticed that the theoretical studies on LRV have begun since the 1980s. In a weakly nonlinear tidal system, the LRV can be represented by its first order approximation, i.e., the mass transport velocity (MTV), which is the sum of ERV and the Stokes' drift velocity (Feng, 1987). This approach has been applied for many coastal and estuarine bays, like the Bohai Sea (Wei et al., 2004), the Gulf of California (Rodríguez et al., 2017) and so on (Tarya et al., 2010; Correia et al., 2020). In recent years, several trials have been carried out on the LRV, such as the derivation of the analytical solution of LRV for an idealized model bay (Jiang and Feng, 2011, 2014; Chen et al., 2020), laboratory studies based on the particle image velocimetry (PIV) technology (Chen et al., 2017; van Gent et al., 2017), and also to investigations of the accumulative effects of turbulent mixing on the residual timescale (Deng et al., 2017). Besides, the Lagrangian tidally-mean theory has been gradually developed from the weakly nonlinear to the generally nonlinear conditions (Ju et al., 2009).

In this work, the LRV structure in the inner Xiangshan Bay is described first based on *in-situ* observation data and second on the major driving forces diagnostically analyzed in the framework of the Lagrangian tidally-mean theory. Data description is presented in Section 2. Section 3 displays results of surface LRV using drifters and MTV below surface based on mooring data. The dynamic analysis of data and general discussion are given in Section 4 and the last section concludes the whole research.

2 Observation and data processing

2.1 *Mooring observations*

The hydrographic data presented in this study were mainly acquired during the spring tide of September 2011 and neap tide of December 2012, respectively. Both data collection cruises lasted over 25 h, including bottom-mounted quadrapods equipped with an up-looking acoustic Doppler current profiler (ADCP) to measure current profiles and a conductivity-temperature-depth (CTD) sensor to record sea surface elevation and pressure, as well as another CTD to monitor the hourly profiles of temperature and salinity. The sensor of ADCP was 0.5 m above the sea bottom, while the height of the bottom-mounted CTD was 0.1 m. For each cruise, three bottom-mounted quadrapods were deployed at Stas B1 to B3 (Fig. 1b). All stations were located in the main channel with an average water depth of over 9 m. Unluckily, data collection failed at Sta. B1 in 2011 and Sta. B3 in 2012, due to the tilt of a quadropod. As a result, data from only two stations in each cruise could be analyzed, as summarized in Table 1.

The RDI 600K/1200K ADCPs were set to record the velocities with a ping rate of 2 Hz. The bin size of the two ADCPs was set to 0.5 m and 0.1 m, respectively and the data were ensemble-averaged over 2 s and 1 s, respectively. The XR420 CTDs were set to continuously collect bottom temperature, salinity and pressure data at a frequency of 1 Hz. For the profile measurement, XR620/420/SBE25 CTDs with sampling frequency of 6 Hz/1 Hz/8 Hz were launched every hour.

2.2 *GPS-GPRS drifters*

Design and initial tests of the surface drifters can be found in Mao et al. (2013). Each drifter consists of a micro controller unit (MCU), a positioning device based on the Global Positioning System (GPS), a communication device based on the General Packet Radio Service (GPRS), Ni-Cd batteries, a bracket and balance weight (Fig. 2). Drifters show a good stability and water-following capability. The location error is estimated at around 30–40 m. When released at the sea surface, the drifter saves its position every 3–5 min and uploads all data to a server through the GPRS communication at 15-min intervals. After the server responds to the drifter, the working cycle is over. Uploaded data include time,

Table 1. Informations and instrumentations at the three observation stations

Station ID	Location	Depth/m	Instrumentation	
			Sept. 14th 12:00–15th 13:00, 2011	Dec. 19th 11:00–20th 12:00, 2012
B1	29.492°N, 121.513°E	9.0	×	RDI 1200K ADCP
				RBR XR420 CTD
				RBR XR420 CTD
B2	29.502°N, 121.558°E	11.6	RDI 600K ADCP	RDI 600K ADCP
			RBR XR420 CTD	RBR XR420 CTD
			RBR XR620 CTD	SBE25 CTD
B3	29.511°N, 121.651°E	12.6	RDI 600K ADCP	×
			RBR XR420 CTD	
			RBR XR620 CTD	

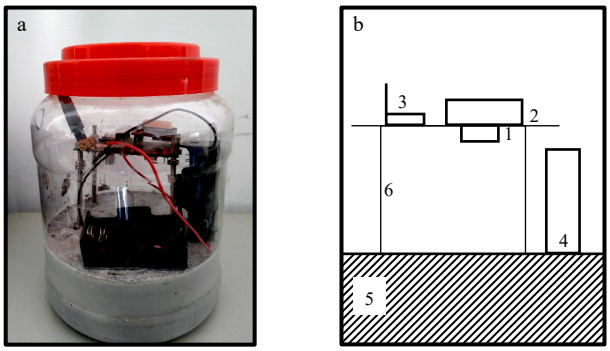

Fig. 2. The sample (a) and section sketch (b) of the GPS-GPRS drifter bottle. Numbers 1–6 in the b denote micro controller (MCU), positioning device GPS, communication device GPRS, Ni-Cd batteries, balance weight and bracket, respectively.

location, and remaining battery power, etc. Data can be displayed on the receiving terminal overlaid with a base map (figures not shown). According to the anemometer observation in December 2012, the wind speed was in the range of 0.5 m/s to 2.0 m/s. Considering the windless condition in the Xiangshan Bay, the drifters could be quite properly released in the area.

GPS-GPRS drifters were released from the mooring stations during the cruises of September 2011 and December 2012, respectively (Table 2). More than half of the released drifters can function longer than 13 h. Quality control of the time-series of the drifter locations is indispensable and is based on three steps. Firstly, drifters that were caught in the aquaculture facilities or floated to shore would be removed. Secondly, the total record length of one drifter should be longer than a M_2 tidal cycle (12.4 h). Thirdly, two adjacent recordings should be continuous with their time interval being shorter than 15 min. Fourthly, considering

Table 2. Parameters of two sets of GPS-GPRS drifter deployments

Duration	Numbers of effective/total drifters	Number of effective trajectories
Sept. 14–15th, 2011	14/28	202
Dec. 19–20th, 2012	17/24	223

that the drifters may be taken out by fishing boats, a drifter's displacement between two adjacent recordings should be less than the product of the maximum tidal current and the time interval. If all these three conditions are met, an effective trajectory during one M_2 tidal cycle could be obtained. In practice, for a drifter with a 15-h length record, e.g., from 01:00 to 16:00, three effective trajectories can be obtained, starting at 01:00, 02:00 and 03:00, respectively. This can describe the LRV at three locations with different initial tidal phases. Figure 3 shows the trajectories of the drifter with maximum and minimum LRV. The maximum LRV (0.266 m/s) was found on April 11, 2012 and the minimum LRV (0.002 m/s) on December 19, 2012.

3 Results

3.1 *Surface LRV pattern*

Based on the effective trajectories, the field of one-M_2-cycle mean LRV for both cruises are shown in Fig. 4. As the tidal current is reversing in the bay, the trajectories are nearly linear along WSW-ENE. The surface LRV is mainly oriented eastward in the central trough and oriented to the head of the bay near the shore, which agrees well to previous research (Jiang and Feng, 2014; Chen et al., 2017; Deng et al., 2017).

During the spring and neap tide, the LRV shows a maximum magnitude of 0.206 m/s and 0.230 m/s, and a mean value of 0.070 m/s and 0.089 m/s, respectively. Although it is one order of magnitude smaller than tidal current, the surface LRV is still sig-

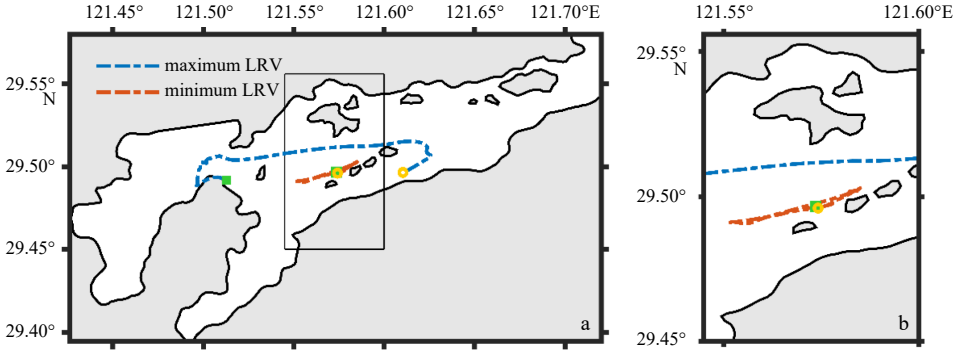

Fig. 3. Drifting trajectories of the drifters with maximum and minimum LRV. b is zooming in the black box of a. Green squares show the released positions and orange circles correspond to the ending points.

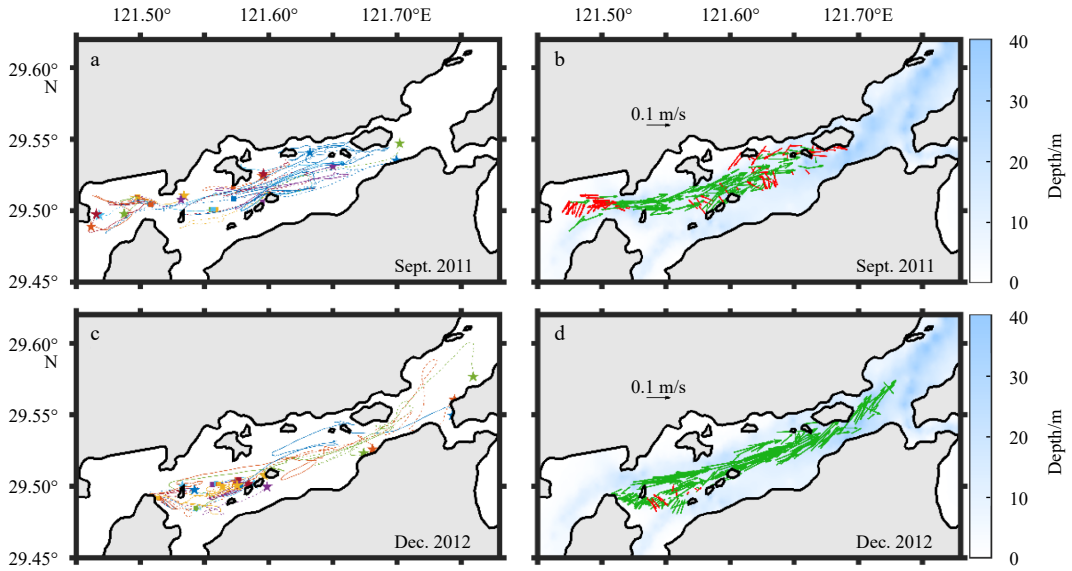

Fig. 4. Trajectories of the drifters (a and c) and the LRV field (b and d) for the two cruises. In a and c, squares represent the released points and stars represent the ending points. In b and d, green arrows mean flowing outwards and red ones mean inflow.

nificant enough in the elongated coastal bay. As for the horizontal distribution, most of stronger LRV occurs in the central trough, while the weaker region near the shore is not so clear. Considering the drifter observation near the shore is limited by the intense aquaculture and fishing facilities, the value of LRV there is meaningless. The maximum and mean LRV are consistent with the order of magnitude observed in the Iroise Sea, France (Muller et al., 2010) and the Bay of Biscay (Charria et al., 2013).

3.2 *Vertical profile of LRV in lower layers*

The LRV below surface cannot be directly obtained from the observation data due to the lack of drifters in the lower layers. However, the profile of MTV can be calculated based on the mooring data and it can approximately take place of LRV in a weakly nonlinear system. For the three stations, the ratio of tidal range to water depth was estimated as 0.201, 0.190 and 0.175, respectively, suggesting a weakly advective nonlinearity. As a result, the vertical profile of LRV can be representative by the MTV ($\boldsymbol{u}_{\mathrm{L}}$).

$$\boldsymbol{u}_{\mathrm{L}} = \boldsymbol{u}_{\mathrm{E}} + \boldsymbol{u}_{\mathrm{S}}, \tag{1}$$

where $\boldsymbol{u}_{\mathrm{E}} = \langle \boldsymbol{u}(\boldsymbol{x}_0, t) \rangle$, and $\boldsymbol{u}_{\mathrm{S}}$ is the Stokes drift velocity which can be calculated as follows:

$$\boldsymbol{u}_{\mathrm{S}} = (u_{\mathrm{S}}, v_{\mathrm{S}}, w_{\mathrm{S}}) = \left\langle \int_{t_0}^{t} \boldsymbol{u}(\boldsymbol{x}_0, t')\,\mathrm{d}t' \cdot \nabla \boldsymbol{u}(\boldsymbol{x}_0, t) \right\rangle, \tag{2}$$

where angle brackets correspond to tidally averaging at a fixed spatial point.

$$\langle A \rangle = \frac{1}{nT} \int_{t_0}^{t_0+nT} A(\boldsymbol{x}_0, t)\,\mathrm{d}t,$$

where $\boldsymbol{x}_0 = \boldsymbol{x}_0(x_0, y_0, z_0)$, t_0 is the initial tidal phase, T is the tidal period and nT means n tidal cycles. In this study, n=1.

It is noticeable that the calculation of MTV requires the spatial gradient of the tidal currents at two stations at least, thus only the MTV profile at Sta. B2 during the spring and neap tides can be obtained, for it is the one station observed in both cruises.

After rotation of the east and north components of ADCP data to lengthways and crossways of the Xiangshan Bay, the crossways component is found to be too weak, as well as the vertical component. Therefore, only lengthways component is analyzed in the following section. The crossways variation $\left(\frac{\partial}{\partial y}\right)$ of any variables in Eq. (2) is also ignored. Equation (1) is finally simplified as follows:

$$u_{\mathrm{L}} = \langle u(\boldsymbol{x}_0, t) \rangle + \left\langle \int_{t_0}^{t} u(\boldsymbol{x}_0, t')\,\mathrm{d}t' \cdot \frac{\partial u(\boldsymbol{x}_0, t)}{\partial x} \right\rangle. \tag{3}$$

As the valid data of the ADCP is far away from both the surface and bottom, the LRV profile in the middle layer is shown in Fig. 5. For the spring-tide condition, lengthways component of the MTV is oriented to the head of the bay at 2–7 m height above the seabed. It is reduced from 0.02 m/s to nearly 0 at a greater height and tends to reversion. It is inferred to be joint well with the surface LRV which is oriented to the bay mouth. For the neap-tide condition, lengthways component is oriented to the bay mouth at 4.0–7.5 m height above the seabed. It decreases from 0.035 m/s at 7.5 m to 0.005 m/s at 4.0 m showing a similar decreasing tendency and also a possible reverse to the head near the seabed. For both cruises, the vertical profiles of LRV at the trough in the inner Xiangshan Bay display the same feature of outflow at the surface and inflow in the deep layer, agreeing well with previous studies such as Cao et al. (1995), Dong and Su (2000) and Zhu (2009). The main difference between the two tidal conditions is that the reversion depth of LRV is shallower for the spring tide than that for the neap tide. It can well explain the phenomenon mentioned in Gao et al. (1990) that the inward net sediment transport during the spring tide is much more than that during the neap tide.

4 Discussion on LRV dynamics

Generally speaking, the vertical pattern of outflow at surface and inflow at bottom is characteristic of gravitational circulation in the coastal estuaries, which is induced by horizontal gradient of the density (Hansen and Rattray, 1965). Although there are

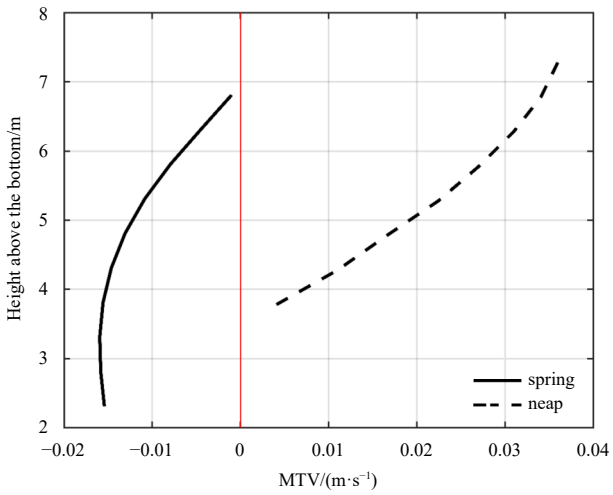

Fig. 5. Vertical profiles of MTV at Sta. B2, with solid line for the spring-tide condition and dashed line for the neap-tide condition. Positive value means outflow and negative indicates inflow, respectively.

more than 50 outlets in the Xiangshan Bay, the riverine runoff is quite weak. The largest flow is estimated at only 130×10^6 m^3/a occurred at the Fuxi River (Fig. 1b) and its flow velocity is about 7–8 cm/s (Fei and Liu, 2018). It hardly induces a significant density gradient and drives baroclinic flow. Therefore, the dynamics of the residual current in the Xiangshan Bay will be analyzed from another aspect based on Lagrangian tidally mean theory in weakly nonlinear tidal system.

4.1 *Governing equations of the MTV*

The 3-D governing equations of MTV in the weakly nonlinear condition are first proposed by Feng (1987). Cui et al. (2019) numerically solved the 3-D equations for an idealized bay for the first time. Considering the bathymetry and tidal current features, the equations in Cui et al. (2019) can be simplified from three aspects in the Xiangshan Bay. First, the crossways and vertical equations of MTV can be neglected, due to the dominant reversing tidal current. In other words, the motion is two dimensional on a *xOz* plane. Second, the Coriolis effect can be neglected because the characteristic Rossby number is much larger than $o(1)$. Third, as the wind is nearly calm during the two cruises, the effect of wind force can be neglected, too. As a result, the equations used for the diagnostic analysis are as follows:

$$0 = -g\frac{\partial\langle\zeta\rangle}{\partial x} - \frac{g}{\langle\rho_0\rangle}\frac{\partial}{\partial x}\int_z^0\langle\rho-\rho_0\rangle\,\mathrm{d}z' + \frac{\partial}{\partial z}\left(A_\mathrm{L}\frac{\partial u_\mathrm{L}}{\partial z}\right) + \pi, \quad (4)$$

where

$$\pi = -\frac{\partial}{\partial z}\left(\langle A_z\rangle\frac{\partial u_s}{\partial z}\right) - \left\langle u\frac{\partial u}{\partial x}\right\rangle. \quad (5)$$

Boundary conditions are as follows:

$$\begin{cases} z=0, & \dfrac{\partial u_\mathrm{L}}{\partial z}=0 \\ z=-h_\mathrm{b}, & u_\mathrm{L}=0 \end{cases},$$

where z=0 is the sea surface, and upward is positive, z=$-h_\mathrm{b}$ is the sea bed; g and ζ represents the gravitational acceleration and water elevation, respectively; ρ is the density, ρ_0 is the reference density; and A_L is vertical eddy viscosity of the residual current. π expressed in Eq. (5) is the tidal body force, named by Feng (1987). The first three terms in the right-hand side of Eq. (4) represent the tidally-averaged barotropic pressure gradient force (BTPGF), baroclinic pressure gradient force (BCPGF) and turbulent stress, respectively. Limited by the data quality, the diagnostic analysis is carried out based only on data of the spring tide, from 12:00 on Sept. 14th to 01:00 on Sept. 15th, 2011.

4.2 *Diagnostic analysis*

4.2.1 *Tidally-averaged pressure gradient forces*

Based on the hourly CTD profile data, the vertical profiles of density at Stas B2 and B3 can be obtained (Fig. 6a). Density was mixed well vertically most of the time except for the ebbing tide when the density difference between surface and bottom was no more than 0.06 kg/m^3. Therefore, the Xiangshan Bay is believed to be a well-mixed coastal bay. After tidally averaged, the horizontal difference of the density changes a little (about 0.14 kg/m^3 at Stas B2 and B3) with depth (Fig. 6b), thus BCPGF in Eq. (4) can be rewritten as follows:

$$-\frac{g}{\langle\bar{\rho}_\mathrm{B2}\rangle}\frac{\langle\bar{\rho}_\mathrm{B3}\rangle-\langle\bar{\rho}_\mathrm{B2}\rangle}{\Delta x}(-z),$$

where $\langle\bar{\rho}_\mathrm{B2}\rangle$ and $\langle\bar{\rho}_\mathrm{B3}\rangle$ correspond to the tidally-averaged vertically-mean density of Stas B2 and B3 and the former one is related

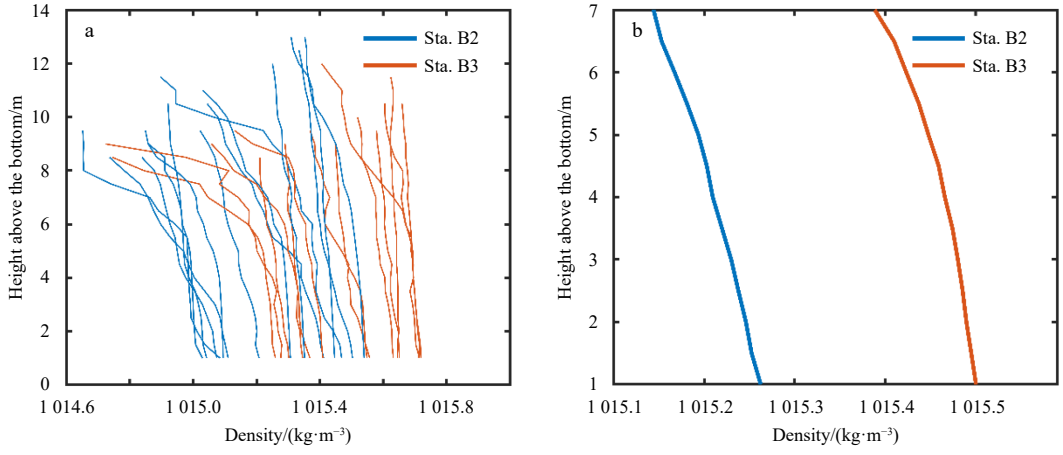

Fig. 6. Hourly (a) and tidally-averaged (b) vertical profiles of density at Stas B2 (blue) and B3 (red).

to the reference density.

Figure 7 shows the tidally-averaged BCPGF varies linearly in the range of -1.19×10^{-6} m/s^2 to -2.75×10^{-6} m/s^2 vertically, one order of magnitude smaller than the BCPGF which can induce gravitational circulation in the tidal estuary (Geyer et al., 2000; Stacey et al., 2010; Basdurak and Valle-Levinson, 2012). This is mainly because of the weak horizontal gradient of density at Sta. B2, which is 2.53×10^{-5} kg/m^3, also one order of magnitude smaller than that of a general tidal estuary (Sharples et al., 1994; Winant and de Velasco, 2003; Simpson et al., 2005).

To obtain the BTPGF at Sta. B2, the calculation is referred to Geyer et al. (2000). Bottom pressure data with 10 min interval from CTD at two stations are indispensable. First, pressure at Sta. B3 (with depth of 12.6 m) should remove the hydrostatic contribution between 11.6 m and 12.6 m, for its depth is 1 m greater than Sta. B2. Subsequently time-series of primary bottom pressure gradient force (PGF) at Sta. B2 can be calculated. Considering the local geopotential surface at two stations are unknown, the primary bottom PGF needs further rectification by use of the vertically integrated momentum equation. If neglecting the surface wind stress, the equation can be rewritten as follows:

$$\tau_{\text{bottom}} = -\int_{-h_b}^{\zeta}\left(\rho\frac{\partial u}{\partial t}+\rho u\frac{\partial u}{\partial x}+\frac{\partial p}{\partial x}\right)\mathrm{d}z, \tag{6}$$

where τ_{bottom} corresponds to the bottom stress. Supposing the bottom stress is zero when the bottom water is motionless, the PGF at that moment (motionless one) can be obtained, as well as the offset between the motionless and primary PGFs. Assuming the offset is invariant with time, the rectified bottom PGF at any moment can be further obtained. Finally, by subtracting the bottom BCPGF from the rectified PGF, the BTPGF can be obtained and is independent of depth. Calculation showed the tidally-averaged BTPGF is -1.64×10^{-5} m/s^2, one order of magnitude larger than BCPGF. Therefore, the gravitation circulation induced by the BCPGF cannot be considered as the dominant dynamics in the Xiangshan Bay.

4.2.2 *Dynamic mechanisms of MTV*

Based on Eqs (2) and (5), the tidal body force can be obtained (Fig. 8). It changes in the range of -0.48×10^{-5} m^2/s to -2.02×10^{-5} m^2/s. The vertical feature is stronger than the PGFs in Eq. (4). To keep

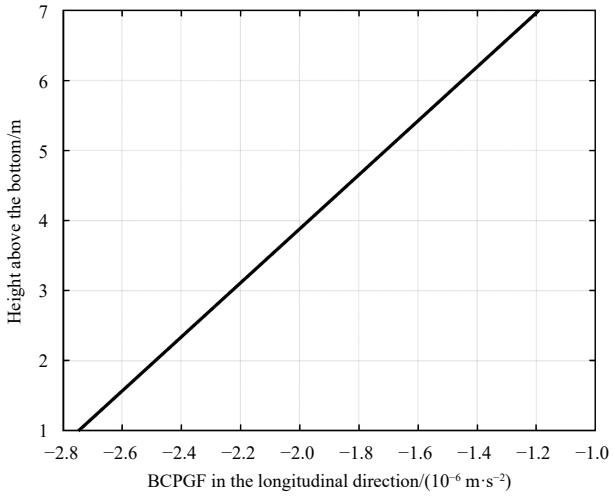

Fig. 7. Vertical profile of tidally-averaged BCPGF at Sta. B2 for the spring-tide condition.

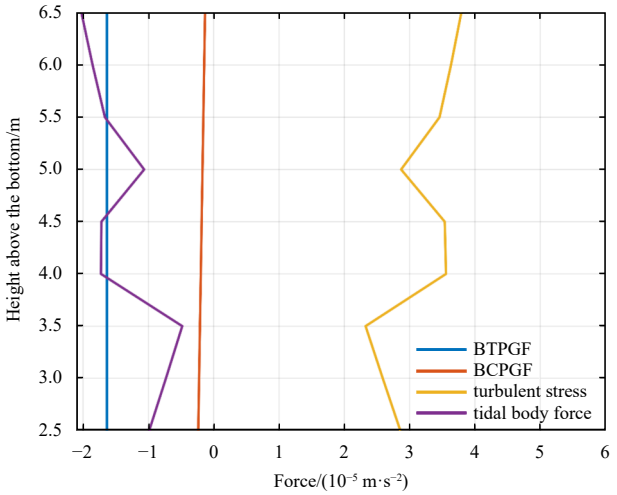

Fig. 8. Vertical profiles of four terms in the MTV governing equation at Sta. B2 for the spring-tide condition.

the balance of MTV governing equation, the tidally-averaged turbulent stress is inferred by the results of the other terms of Eq. (4). Figure 8 shows clearly that the three dynamic factors, tidally-averaged BTPGF, tidally-averaged turbulent stress and tidal body force are comparable in the inner Xiangshan Bay. By contrast, the tidally-averaged BCPGF can be neglectable, for it is one order smaller. It can be further concluded that the residual circulation in the central trough of the inner Xiangshan Bay is controlled by a quasi-barotropic tide-induced residual current rather by the baroclinic gravitational circulation.

4.3 *Theoretical result of tidally-averaged turbulent stress*

As A_L in the third term of Eq. (4) is unknown, the tidally-averaged turbulent stress can only be inferred from the other terms. In reality, A_L is usually expressed as the tidally-averaged vertical eddy viscosity $\langle A_z\rangle$ (Cui et al., 2019; Chen et al., 2020). In this section, we will try to calculate the tidally-averaged turbulent stress by expression of $\langle A_z\rangle$. Two methods can be used to obtain A_z from the observation data: the "variance method" (Lu and Lueck, 1999; Stacey et al., 1999) and the dynamic balance method. According to the "variance method", Reynolds stress can be firstly calculated from ADCP along-beam velocities and A_z can be subsequently obtained. Unfortunately, the along-beam velocities at Sta. B2 for the cruise of Sept., 2011 were invalid due to the bad ADCP attitude and overlarge pitch and roll angles. As a result, only dynamic balance method can be used to calculate the vertical eddy viscosity. If neglecting the surface wind stress, $A_z(z, t)$ can be expressed as Eq. (7):

$$A_z(z,t) = -\frac{\int_z^{\zeta}\left[\frac{\partial u}{\partial t}+u\frac{\partial u}{\partial x}+g\frac{\partial \zeta}{\partial x}+\frac{g}{\rho_0}\frac{\partial \rho}{\partial x}(\zeta-z')\right]\mathrm{d}z'}{\frac{\partial u}{\partial z}}. \tag{7}$$

Result reveals an obvious flood-dominant asymmetry, thus the tidally-averaged vertical curve of $\langle A_z\rangle$ is similar to the maximum during the flood tide (Fig. 9). It varies in the range of 0.2×10^{-2} m^2/s to 1.2×10^{-2} m^2/s, in agreement with that in Xu et al. (2017). Connected with the vertical shear of MTV, the tidally-averaged turbulent stress in the Eq. (4) can be obtained. It varies from -2.39×10^{-5} to 2.19×10^{-5} m/s^2, the same order of magnitude as BT-

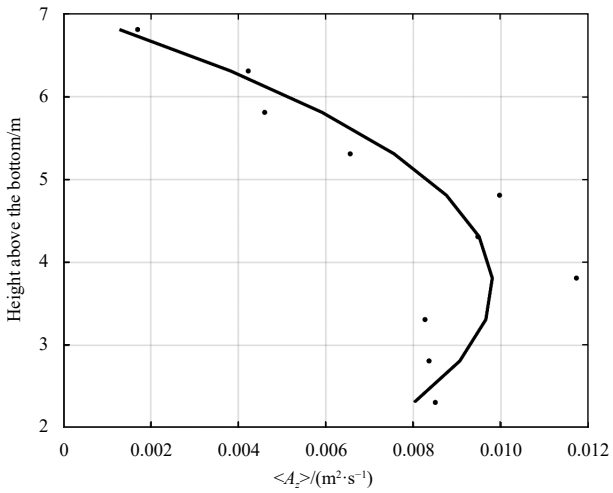

Fig. 9. Scatter diagram and fitting vertical curves of tidally-averaged vertical eddy viscosity at Sta. B2 for the spring-tide condition.

PGF. In the vertical, it firstly increases and then decreases with increasing height, reversing at 5 m height above the seabed and keeping increasing after that (Fig. 10).

By comparing two curves of tidally-averaged turbulent stress in Figs 8 and 10, it should be noted that replacing A_L by $\langle A_z \rangle$ in Eq. (4) might be improper, for the result cannot guarantee the balance of equation. It is also probably related to the numerical errors brought by interpolation and integration. In any case, how to express the effect of turbulent on the residual current is an open-ended question and needs further work.

5 Conclusions

Based on the observation data during spring and neap tide cruises in the inner Xiangshan Bay, China, the LRV and its dynamic mechanism were analyzed. Results of the GPS-GPRS surface drifters show that surface LRV flows outwards in the deep trough and flows inward near the shoreside. The mean value of LRV in spring and neap tide is 0.070 m/s and 0.089 m/s, respectively. As for the LRV below surface, the mooring data were used to deduce the vertical profile. It outflows at the surface and inflows in the deep layer, agreeing well with the gravitational circulation in a typical estuary. However, these dynamics are not based on a baroclinic effect at all. All terms in the MTV governing equation are diagnostically calculated from the mooring data. The main forces driving the LRV in the inner bay are the tidally-averaged BTPGF, tidally-averaged turbulent stress and tidal body force, showing that the major dynamic is barotropic. Additionally, it is found that when the tidally-averaged turbulent stress is calculated according to its definition, the value is quite different from the one deducted from the MTV equation. Besides the calculation error, its expression may also need to be improved.

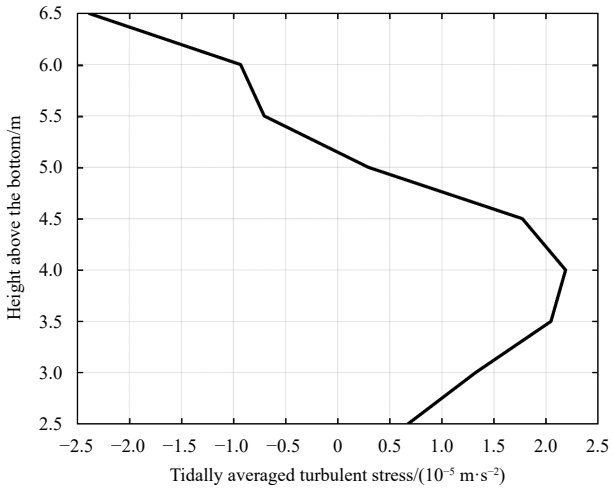

Fig. 10. Vertical profile of the theoretical tidally-averaged turbulent stress at Sta. B2 for the spring-tide condition.

References

Abbott M R. 1960. Boundary layer effects in estuaries. Journal of Marine Research, 18: 83–100

Balsells M F P, Grifoll M, Espino M, et al. 2020. Wind-driven hydrodynamics in the shallow, micro-tidal estuary at the Fangar Bay (Ebro Delta, NW Mediterranean Sea). Applied Sciences, 10(19): 6952, doi: 10.3390/app10196952

Basdurak N B, Valle-Levinson A. 2012. Influence of advective accelerations on estuarine exchange at a Chesapeake Bay tributary. Journal of Physical Oceanography, 42(10): 1617–1634, doi: 10.1175/JPO-D-11-0134.1

Callies U, Groll N, Horstmann J, et al. 2017. Surface drifters in the German Bight: Model validation considering windage and Stokes drift. Ocean Science, 13(5): 799–827, doi: 10.5194/os-13-799-2017

Cao Xinzhong, Tang Longmei, Zhang Yuexiu. 1995. Analyses of the hydrography features and the ability for containing contaminator for Port Xiangshan. Donghai Marine Science, 13(1): 10–19

Charria G, Lazure P, Le Cann B, et al. 2013. Surface layer circulation derived from Lagrangian drifters in the Bay of Biscay. Journal of Marine Systems, 109–110 Suppl: S60–S76, doi: 10.1016/j.jmarsys.2011.09.015

Chen Yang, Cui Yanxing, Sheng Xiaoxuan, et al. 2020. Analytical solution to the 3D tide-induced Lagrangian residual current in a narrow bay with vertically varying eddy viscosity coefficient. Ocean Dynamics, 70(6): 759–770, doi: 10.1007/s10236-020-01359-3

Chen Yang, Jiang Wensheng, Chen Xu, et al. 2017. Laboratory experiment on the 3D tide-induced Lagrangian residual current using the PIV technique. Ocean Dynamics, 67(12): 1567–1576, doi: 10.1007/s10236-017-1108-6

Chen Minglong, Jin Meng, Tao Peiran, et al. 2018. Assessment of microplastics derived from mariculture in Xiangshan Bay, China. Environmental Pollution, 242: 1146–1156, doi: 10.1016/j.envpol.2018.07.133

Chen Minmo, Zhu Zenan, Zhang Chuanzheng, et al. 2021. Mapping of tidal current and associated nonlinear currents in the Xiangshan Bay by coastal acoustic tomography. Ocean Dynamics, 71(8): 811–821, doi: 10.1007/s10236-021-01470-z

Cheng Peng. 2020. On residual velocities in sigma coordinates in narrow tidal channels. Acta Oceanologica Sinica, 39(5): 1–10, doi: 10.1007/s13131-020-1579-z

Clarke A J, Van Gorder S. 2018. The relationship of near-surface flow, stokes drift and the wind stress. Journal of Geophysical Research: Oceans, 123(7): 4680–4692, doi: 10.1029/2018JC014102

Correia C, Torres A F, Rosa A, et al. 2020. Export of dissolved and suspended matter from the main estuaries in South Portugal during winter conditions. Marine Chemistry, 224: 103827, doi: 10.1016/j.marchem.2020.103827

Cui Yanxing, Jiang Wensheng, Deng Fangjing. 2019. 3D numerical computation of the tidally induced Lagrangian residual current in an idealized bay. Ocean Dynamics, 69(3): 283–300, doi: 10.1007/s10236-018-01243-1

Delhez E J M. 1996. On the residual advection of passive constituents. Journal of Marine Systems, 8(3/4): 147–169, doi: 10.1016/0924-7963(96)00004-8

Deng Fangjing, Jiang Wensheng, Feng Shizuo. 2017. The nonlinear

effects of the eddy viscosity and the bottom friction on the Lagrangian residual velocity in a narrow model bay. Ocean Dynamics, 67(9): 1105–1118, doi: 10.1007/s10236-017-1076-x

Dong Lixian, Su Jilan. 2000. Salinity distribution and mixing in Xiangshangang Bay: I. Salinity distribution and circulation pattern. Oceanologia et Limnologia Sinica, 31(2): 151–158

Fei Yuejun, Liu Lian. 2018. Applied Research on Rotal Amount Control and Emission Reduction Assessment of Pollutants in Xiangshan Bay. Beijing: China Ocean Press, 64–65

Feng Shizuo. 1987. A three-dimensional weakly nonlinear model of tide-induced Lagrangian residual current and mass transport, with an application to the Bohai Sea. In: Nihoul J C J, Jamart B M, eds. Three Dimensional models of Marine and Estuarine Dynamics. Elsevier Oceanography Series. v45. Amsterdam, the Netherlands: Elsewier, 471–488, doi: 10.1016/S0422-9894(08)70463-X

Feng Shizuo, Ju Lian, Jiang Wensheng. 2008. A Lagrangian mean theory on coastal sea circulation with inter-tidal transports: I. Fundamentals. Acta Oceanologica Sinica, 27(6): 1–16

Gao Shu, Xie Qinchun, Feng Yingjun. 1990. Fine-grained sediment transport and sorting by tidal exchange in Xiangshan Bay, Zhejiang, China. Estuarine, Coastal and Shelf Science, 31(4): 397–409, doi: 10.1016/0272-7714(90)90034-O

Geyer W R, Trowbridge J H, Bowen M M. 2000. The dynamics of a partially mixed estuary. Journal of Physical Oceanography, 30(8): 2035–2048, doi: 10.1175/1520-0485(2000)030<2035:TDOAPM>2.0.CO;2

Haid V, Stanev E V, Pein J, et al. 2020. Secondary circulation in shallow ocean straits: observations and numerical modeling of the Danish Straits. Ocean Modelling, 148: 101585, doi: 10.1016/j.ocemod.2020.101585

Han Songlin, Liang Shuxiu, Sun Zhaochen. 2014. Numerical simulation of tides, tidal currents and temperature-salinity structures in Xiangshan Bay based on FVCOM. Journal of Waterway and Harbor, 35(5): 481–488

Hansen D V, Rattray M. 1965. Gravitational circulation in straits and estuaries. Journal of Marine Research, 23(2): 104–122

Hill A E, Brown J, Fernand L, et al. 2008. Thermohaline circulation of shallow tidal seas. Geophysical Research Letters, 35(11): L11605, doi: 10.1029/2008GL033459

Huijts K M H, Schuttelaars H M, de Swart H E, et al. 2009. Analytical study of the transverse distribution of along-channel and transverse residual flows in tidal estuaries. Continental Shelf Research, 29(1): 89–100, doi: 10.1016/j.csr.2007.09.007

Jiang Wensheng, Feng Shizuo. 2011. Analytical solution for the tidally induced Lagrangian residual current in a narrow bay. Ocean Dynamics, 61(4): 543–558, doi: 10.1007/s10236-011-0381-z

Jiang Wensheng, Feng Shizuo. 2014. 3D analytical solution to the tidally induced Lagrangian residual current equations in a narrow bay. Ocean Dynamics, 64(8): 1073–1091, doi: 10.1007/s10236-014-0738-1

Jiang Wensheng, Sun Wenxin. 2002. Three dimensional tide-induced circulation model on a triangular mesh. International Journal for Numerical Methods in Fluids, 38(6): 555–566, doi: 10.1002/fld.231

Ju Lian, Jiang Wensheng, Feng Shizuo. 2009. A Lagrangian mean theory on coastal sea circulation with inter-tidal transports: II. Numerical experiments. Acta Oceanologica Sinica, 28(1): 1–14

Lavelle J W, Cokelet E D, Cannon G A. 1991. A model study of density intrusions into and circulation within a deep, silled estuary: Puget Sound. Journal of Geophysical Research: Oceans, 96(C9): 16779–16800, doi: 10.1029/91JC01450

Liang Shuxiu, Han Songlin, Sun Zhaochen, et al. 2014. Lagrangian methods for water transport processes in a long-narrow bay—Xiangshan Bay, China. Journal of Hydrodynamics, 26(4): 558–567, doi: 10.1016/S1001-6058(14)60063-9

Liu Qiang, Xu Xiaoqun, Zeng Jiangning, et al. 2019. Heavy metal concentrations in commercial marine organisms from Xiangshan Bay, China, and the potential health risks. Marine Pollution Bulletin, 141: 215–226, doi: 10.1016/j.marpolbul.2019.02.058

Lu Youyu, Lueck R G. 1999. Using a broadband ADCP in a tidal channel. Part I: Mean flow and shear. Journal of Atmospheric and Oceanic Technology, 16(11): 1556–1567, doi: 10.1175/1520-0426(1999)016<1556:UABAIA>2.0.CO;2

Mao Xinyan, Zhao Liang, Xu Peng, et al. 2013. Coastal GPS-GPRS drifting path observation system and its application. Periodical of Ocean University of China, 43(9): 12–16

Muller H, Blanke B, Dumas F, et al. 2010. Identification of typical scenarios for the surface Lagrangian residual circulation in the Iroise Sea. Journal of Geophysical Research: Oceans, 115(C7): C07008, doi: 10.1029/2009JC005834

Rodríguez P A, Carbajal N, Rodríguez J H G. 2017. Lagrangian trajectories, residual currents and rectification process in the Northern Gulf of California. Estuarine, Coastal and Shelf Science, 194: 263–275, doi: 10.1016/j.ecss.2017.06.019

Röhrs J, Christensen K H, Hole L R, et al. 2012. Observation-based evaluation of surface wave effects on currents and trajectory forecasts. Ocean Dynamics, 62(10–12): 1519–1533, doi: 10.1007/s10236-012-0576-y

Schulz K, Umlauf L. 2016. Residual transport of suspended material by tidal straining near sloping topography. Journal of Physical Oceanography, 46(7): 2083–2102, doi: 10.1175/JPO-D-15-0218.1

Sharples J, Simpson J H, Brubaker J M. 1994. Observations and modelling of periodic stratification in the upper York River Estuary, Virginia. Estuarine, Coastal and Shelf Science, 38(3): 301–312, doi: 10.1006/ecss.1994.1021

Simpson J H, Williams E, Brasseur L H, et al. 2005. The impact of tidal straining on the cycle of turbulence in a partially stratified estuary. Continental Shelf Research, 25(1): 51–64, doi: 10.1016/j.csr.2004.08.003

Stacey M T, Brennan M L, Burau J R, et al. 2010. The tidally averaged momentum balance in a partially and periodically stratified estuary. Journal of Physical Oceanography, 40(11): 2418–2434, doi: 10.1175/2010JPO4389.1

Stacey M T, Monismith S G, Burau J R. 1999. Measurements of Reynolds stress profiles in unstratified tidal flow. Journal of Geophysical Research: Oceans, 104(C5): 10933–10949, doi: 10.1029/1998JC900095

Stashchuk N, Vlasenko V, Hosegood P, et al. 2017. Tidally induced residual current over the Malin Sea continental slope. Continental Shelf Research, 139: 21–34, doi: 10.1016/j.csr.2017.03.010

Sun Weiping, Yu Jianjun, Xu Xiaoqun, et al. 2014. Distribution and sources of heavy metals in the sediment of Xiangshan Bay. Acta Oceanologica Sinica, 33(4): 101–107, doi: 10.1007/s13131-014-0456-z

Tamtare T, Dumont D, Chavanne C. 2021. The stokes drift in ocean surface drift prediction. Journal of Operational Oceanography, 1–13, doi: 10.1080/1755876X.2021.1872229

Tarya A, Hoitink A J F, Van der Vegt M. 2010. Tidal and subtidal flow patterns on a tropical continental shelf semi-insulated by coral reefs. Journal of Geophysical Research: Oceans, 115(C9): C09029, doi: 10.1029/2010JC006168

van Gent P L, Michaelis D, van Oudheusden B W, et al. 2017. Comparative assessment of pressure field reconstructions from particle image velocimetry measurements and Lagrangian particle tracking. Experiments in Fluids, 58(4): 33, doi: 10.1007/s00348-017-2324-z

Wan Meng, Yao Yanming, Chen Qin, et al. 2015. Numerical simulation study on the residual currents in the Xiangshan Bay. Marine Science Bulletin, 34(3): 295–302

Wei Hao, Hainbucher D, Pohlmann T, et al. 2004. Tidal-induced Lagrangian and Eulerian mean circulation in the Bohai Sea. Journal of Marine Systems, 44(3/4): 141–151, doi: 10.1016/j.jmarsys.2003.09.007

Winant C D, de Velasco G G. 2003. Tidal dynamics and residual circulation in a well-mixed inverse estuary. Journal of Physical Oceanography, 33(7): 1365–1379, doi: 10.1175/1520-0485(2003)033<1365:TDARCI>2.0.CO;2

Xu Peng, Mao Xinyan, Jiang Wensheng. 2016. Mapping tidal residual circulations in the outer Xiangshan Bay using a numerical

model. Journal of Marine Systems, 154: 181–191, doi: 10.1016/j.jmarsys.2015.10.002

Xu Peng, Mao Xinyan, Jiang Wensheng. 2017. Estimation of the bottom stress and bottom drag coefficient in a highly asymmetric tidal bay using three independent methods. Continental Shelf Research, 140: 37–46, doi: 10.1016/j.csr.2017.04.004

Zhao Binfeng, Wang Ximing, Jin Hangbiao, et al. 2018. Spatiotemporal variation and potential risks of seven heavy metals in seawater, sediment, and seafood in Xiangshan Bay, China (2011–2016). Chemosphere, 212: 1163–1171, doi: 10.1016/j.chemosphere.2018.09.020

Zhu Junzheng. 2009. Numerical simulation of characteristic of 3-D tidal flow in Xiangshan Bay. Journal of Hydroelectric Engineering, 28(3): 145–151

Zimmerman J T F. 1979. On the Euler-Lagrange transformation and the Stokes' drift in the presence of oscillatory and residual currents. Deep-Sea Research Part A: Oceanographic Research Papers, 26(5): 505–520, doi: 10.1016/0198-0149(79)90093-1